Feasibility Study for an Ice-Based Image Monitoring System for Polar Regions Using Improved Visual Enhancement Algorithms

Yuchen Wang, Yinke Dou, Jingxue Guo, Zhe Yang, Bo Yang, Yang Sun, and Weixin Liu

***Abstract*—Melting and evolution of Arctic Ocean sea ice in summer are one of the main factors affecting sea ice albedo and climate. At present, remote sensing images of sea ice are mainly acquired with the help of payload platforms, such as aircraft or satellites. The above methods have a large measurement scale and a short period. Sea ice research also requires suitable equipment for fine-scale, visualized long-term tracking observations of target sea ice regions. This article investigates the feasibility of measuring interannual variability in sea ice morphology in the Arctic sea ice environment using a low-power gimbal camera automated by satellite communications. Year-round observational data from the arctic field were used. The sea ice images were defogged and edge-enhanced by a newly developed algorithm with the help of human visual enhancement principles. During the 11th Chinese National Arctic Science Expedition, the system was placed on perennial ice in the northern Beaufort Basin to monitor sea ice appearance changes and the external state of the ice mass balance buoy. The system fuses visually enhanced sea ice images with ice balance buoy data from the same ice floe in a multi-scale environmental sequence to obtain sea ice observations with image sequences. The data complement the need for long-duration, fixed-ice, and short-visual-range observations in sea-ice studies. The equipment design methods and image processing algorithms involved in the experimental process have accumulated engineering experience for this application area. The research methodology provides a new framework for long-term, and visualized sea ice observation methods.**

***Index Terms*—Arctic sea ice, Retinex, satellite communications.**

Manuscript received February 26, 2022; revised April 8, 2022; accepted May 6, 2022. Date of publication May 11, 2022; date of current version May 20, 2022. This work was supported in part by the National Natural Science Foundation of China under Grant 41941007 and in part by the National Natural Science Foundation of China under Grant 42176231. *(Corresponding authors: Yinke Dou; Jingxue Guo.)*

Yuchen Wang is with the College of Electrical and Power Engineering, Taiyuan University of Technology, Taiyuan 030024, China, and also with Zhongshan National Ice and Space Environment Observation and Research Station, Polar Research Institute of China, Shanghai 200136, China (e-mail: tyut_yuchenwang@163.com).

Yinke Dou and Bo Yang are with the College of Electrical and Power Engineering, Taiyuan University of Technology, Taiyuan 030024, China (e-mail: douyk8888cn@126.com; 15835702126@163.com).

Jingxue Guo and Yang Sun are with the Zhongshan National Ice and Space Environment Observation and Research Station, Polar Research Institute of China, Shanghai 200136, China (e-mail: guojingxue@pric.org.cn; sunyang@pric.org.cn).

Zhe Yang is with the School of Information Science and Engineering, Harbin Institute of Technology, Weihai 264209, China (e-mail: jimyz0106@163.com).

Weixin Liu is with the Changning Meteorological Bureau, Changning 678100, China (e-mail: 765231462@qq.com).

Digital Object Identifier 10.1109/JSTARS.2022.3173821

I. Introduction

THE arctic is a crucial component of the Earth's climate system, affecting the energy balance, atmospheric and oceanic circulation, ecology, and natural resources [1], [2]. Arctic sea ice cover is both an indicator and an amplifier of climate change [3]. Changes in sea ice are macroscopically manifested as sea ice thickness and sea ice coverage area. Sea ice thickness affects processes related to arctic climates, such as climate change, freshwater balance and ocean circulation, and maritime security [4]–[6]. Sea ice research is a broad, interdisciplinary scientific topic with many subdisciplines and processes at play [7]. In particular, ice extent, thickness, and age are often used as indicators of climate change. Over the past few decades, Arctic sea ice has changed dramatically, as evidenced by trends such as shrinking ice extent, decreasing ice thickness, replacement of multiyear ice by younger first-year ice, and decreasing ice concentration [8]–[10]. Projections from climate models suggest that a reduction in the extent of summer sea ice could lead to no summer ice in the Arctic for the next 25–30 years [11]. The databases for the above discussion and prediction models are based on various observations obtained *in situ*. There are multiple types of arctic sea ice observation data, broadly classified into two categories according to the observation load platform. One type is remote sensing data with aerial platforms as the central observation platform. The other type is physical sensor data with in-situ sensors such as buoys and submersible sensors as the central observation platform.

Since 1970, satellite optical infrared and microwave sensors have matured as observational tools for cold regions. Optical infrared sensors are well suited for mapping environmental variables over heterogeneous landscapes due to their relatively high resolution (submeter to 1 km). However, the signal-to-noise ratio of the observations may be degraded by cloud atmosphere aerosol contamination, low solar altitude, and prolonged seasonal darkness at high latitudes [12]. Microwave remote sensing is less affected by atmospheric conditions and provides diurnal earth observations in almost all-weather conditions [13]. The two types of observation methods described above are suitable for monitoring large areas of sea ice, but microwave remote sensing does not provide access to atmospheric and oceanic parameters collected by *in situ* sensors on the sea ice being observed. For microwave payloads carried on satellites, the observation time is relatively fixed. Researchers cannot obtain data at a specific

scale at an arbitrary time. Unmanned airborne remote sensing observations were born out of this need. Such platforms provide the flexibility to choose the appropriate data acquisition period and data type (multispectral, hyperspectral, thermal, microwave, and LIDAR) [14]. The advent of lightweight, low-cost UAVs and various remote sensing products has changed the outlook of glaciological research. Due to the continuous thickness variation of Arctic sea ice, drift trajectories and surface morphology observations are limited by remote sensing data's coarse spatial and temporal resolution. Therefore, ground data are needed to validate and complement satellite products [15]. The use of autonomous ice mass balance buoys (IMBs) has dramatically expanded the opportunities for long-term sea ice mass balance observations. These buoys can address local ice mass balance changes by measuring snow depth and time series of ice surface and bottom locations [16].

The first IMB was developed by the US Cold Regions Research and Engineering Laboratory in conjunction with Ocean Weather Canada Ltd. The IMB is anchored to the ice floe at a fixed location, and the buoy makes automated measurements at predetermined intervals along the ice drift track (measurement parameters include ranging acoustic sonar of snow and ice bottom, temperature data from the air-ice-sea profile, and atmospheric parameters) The data are transmitted via the Iridium satellite. This type of IMB is widely used in the arctic ocean [17]. In addition, a high-resolution material balance buoy (Simba) was developed by the Scottish Marine Science Association of the Scottish Marine Institute, U.K. This type of buoy is a basic functional unit to realize the Arctic Ocean buoy observation network grouping. In Liao *et al.*'s study, mathematical and physical-based algorithms were used to process SIMBA temperature data, and the model automatically calculated snow depth and ice thickness [17], [18]. Simba data have been used for monitoring snow depth and ice thickness in seasonally frozen lakes and energy balance studies [19] and polar ocean studies [20], [21].

A vital observation tool is in situ image acquisition of ice and snow and visualization of ice cores after removal. The appearance and disappearance of melting ponds in the arctic and the associated parameters also reflect the seasonal and thermodynamic processes in the ice cover. No mature buoy system can achieve fixed optical camera observations of perennial ice in high-latitude sea ice regions. The combination of morphological sea ice appearance image data from optical cameras working in the central arctic throughout the year, material balance data from IMB buoys, and sea ice light flux data may provide more comprehensive support for explaining sea ice change mechanisms.

In this article, a miniature serial camera was selected as the image acquisition sensor and mounted on a cold and wet-proof head to monitor the surroundings of its location. Filming during extreme nights can be accomplished during the test period. The performance of the sea ice camera was evaluated over an operating temperature range of -40 °C to 10 °C, including signal integrity output, low light conditions output, and defogging image output. These reference attributes support further construction of sea ice refinement research methods. The overall performance of the sea ice camera buoys was evaluated during the 9th and 11th Chinese National Arctic Research Expedition. The methodology employed and the design of this article provides a general framework for this observational tool. This assessment provides a feasibility check for the long-term operation of visible and infrared cameras in arctic sea ice areas, and provides data to support the material balance characteristics corresponding to the changing cycles of sea ice surface morphology.

II. Imaging Systems and Drive Electronics

In the arctic high latitude ice floes, both buoys and marine sensors face multiple tests. Systems with optical imaging capabilities operating on polar sea ice require a higher level of protection than optical systems operating in other common operating conditions, which is the first challenge in the design process of this article. On the Arctic sea ice, the long-duration automated observation equipment deployed by the researchers has less use of motion joints, especially those with movable joints, such as robotic arms and heads. This type of equipment faces seawater corrosion of the kinematic joints and the problem of limited joint movement due to freezing. This is the second challenge that needs to be encountered in the design process of this article; the amount of image data taken by the optical camera at one time is hundreds to thousands of times more than the amount of data observed by an ordinary IMB buoy at one time. The camera and gimbal power consumption for a single observation are higher than other field sea ice observation equipment. If long-term observations are needed, the design of energy planning and data delivery methods becomes one of the biggest challenges in this article.

A. System Composition

Considering the above kind of problems relative to the equipment for the operation in the arctic site, the system is designed in order to face different situations. The whole image monitoring system contains four subsystems, i.e., image acquisition, motion head, renewable energy, and a central controller. Due to the very high relative humidity of the arctic air (i.e., the average annual rate can reach to 85%,and in summer it can reach to 100%) [22], the renewable energy subsystem and the central controller subsystem are encapsulated in a waterproof insulated instrument case with IP67 protection. The motion head is IP66 rated, and the image acquisition subsystem is in the head's enclosure. The optical camera is in the environmental maintenance system inside the head and can work stably during extreme nights at -40 °C.

The overall structure of the system is shown in Fig. 1. The designs with observation functions and the central control system are relatively high in the centre of the whole network. The splashing and erosion of seawater are prevented from affecting the equipment. The photovoltaic (PV) panels are coated with a hydrophobic coating to avoid hang-ups of ice. A triangular façade is used to ensure that snow and ice can slide smoothly when the snowfall is less than the height of the box to ensure the efficiency of the PV output. A square white anti-melting board with a side length of 2 m is used as a flat base for installation, and the functional modules described above are placed on top of this antimelting board. The buck circuit supplies

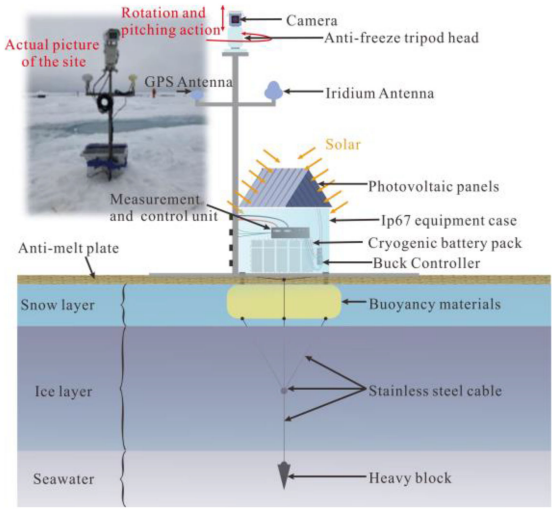

Fig. 1. Schematic diagram of sea ice monitoring system structure.

TABLE I
CAMERA HEAD PARAMETERS

Parameters	Value	Unit
Head level range	0-360	°
Head horizontal speed	0.1~60	°/S
Vertical range of the head	-78~0	°
Head vertical speed	0.1~30	°/S
Power consumption	⩽60	W
Power supply	AC24±25%	V
Product size	340 (L)*165 (W)*371(H)	mm
Head weight	6.8	kg
Load weight	2.5 (including shield)	kg
Working environment temperature	-55~+65	℃
Working environment humidity	<95	%RH

the voltage generated by the PV to the summer battery bank for charging, and the PV output is kept above the threshold for floating voltage to the wintering battery bank to prepare for the extreme night energy supply. The buoyant material on the lower part of the anti-melt plate and the steel cable suspension weight are calculated. The water level remains at the plate position after the sea ice melts into a melt pool.

B. Motion Head and Camera

Each part of the head is customized with specialization, and the specific performance parameters are given in Table I.

The most important of the system's components is the camera section. The designers modified Spinel USA LLC's SC03MPA series cameras inside in order to ensure high definition, low noise and unobstructed images in the central arctic region.

As shown in Fig. 2, mainly heating and lens decontamination functions were added. By adding a servo with a brush head and a lens barrel heating assembly, the designers attempted to remove the small amount of water vapor condensation in the lens that causes unclear shots during operation while also

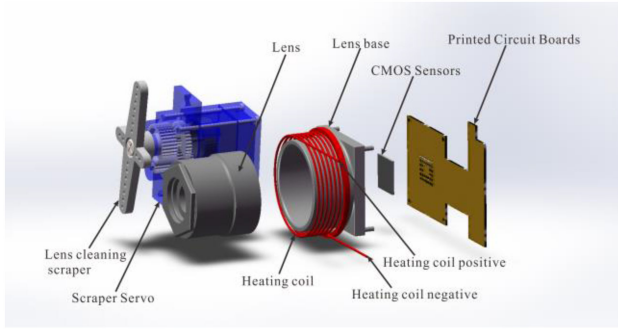

Fig. 2. Camera modification schematic.

TABLE II
IMPROVED CAMERA PARAMETERS

Options	Standard	Custom Options
Image Sensor	1/4" CMOS MT9V011	-----
Resolution	300K Pixels	-----
Image/Video Format	Still JPEG compressed	NTSC/PAL upon request
Image Size (Default)	320x240	640x480, 120x160
Serial Interface	TTL/RS232/RS485	-----
Protocol & Connection	VC0706	-----
Baud Rate (Default)	38400bps	9600bps, 57600bps, and 115200bps
Focus	Fixed	Mannually adjustable
Minimum Illumination	1Lux	-----
Power Supply	DC 5V/3.3V (Default)	12V DC or wide voltage 9-36V
Power Consumption	Typical: 80mA, Max: 100mA	-----
Operating Temp	-40°C~+60°C	-----
Storage Temp	-50°C~+70°C	-----

heating the chip to ensure that chips such as the SP3232E on the board, which require operating temperatures above −30 °C, can function appropriately in ambient temperatures below −30 °C.

The information in Table II shows the relevant electrical parameters of the improved camera.

C. Data Parsing and Return Method

Researchers generally use satellite communication to construct communication links in the equipment placed in the arctic. Some of the closer offshore observation units will use land-based contact, and some of the closer offshore but beacon-capable storage observation units use manual recovery of data readings.

Each year, during the northern hemisphere summer, researchers are able to reach areas north of 83°N by means of vehicles, such as icebreakers or ice-zone carriers and deploy observation instruments on the sea ice. First, the equipment in the area cannot communicate directly through land-based stations. Second, the cost of manual salvage is high and difficult to reach by icebreakers below the PC3 [23] level in some ice areas. Therefore, the observation equipment in the central arctic region is primarily long-duration observation units that can be collected autonomously and can communicate in both directions.

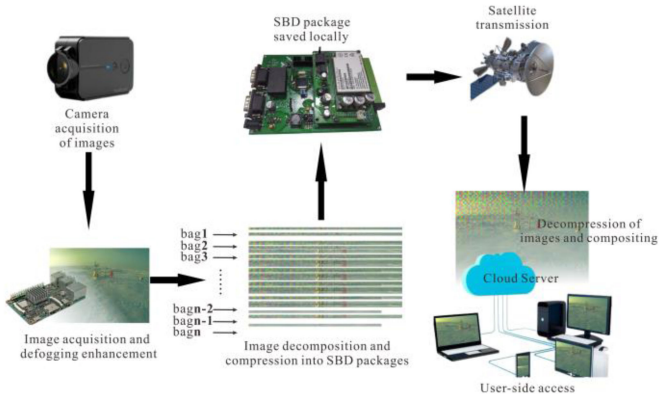

Fig. 3. Introduction of image data transmission principle.

The communication link medium of the arctic ice-based image monitoring system is the satellite communication method. This is shown in Fig. 3. The transmission of images is different from other forms of data transmission. The traditional Transmission Control Protocol/Internet Protocol (TCP/IP) or User Datagram Protocol (UDP) network protocols often suffer from incomplete data due to packet loss in poor network conditions. This situation seriously affects the transmission of sequences with large data volumes and sequencing rules. The integrity of data transmitted by satellite is affected by the method of compression and decompression. The selection of a suitable data compression and decompression method is crucial when transmitting large amounts of bytes of data such as hydroacoustic signals and images in polar regions. The data transmission method of this system is shown in Fig. 3, which can be roughly divided into four parts: data acquisition; data compression and decomposition; data transmission; and data decompression and reconstruction.

The serial camera does the data acquisition process on-site with the moving head. The acquired images are transmitted to the Raspberry Pi part of the central control unit for processing. After image target detection and photo quality monitoring, select whether to carry out the transmission of images. To ensure the quality of the transmitted images, the images are screened by the Raspberry Pi computer before they can be compressed and sent to the satellite. To ensure the continuous operation of the system, the microcontroller, which is more resistant to low temperature, becomes the highest priority decision unit in this system, and the whole system can still complete the image transmission work in case the Raspberry Pi is down. Before the data is transferred to the microcontroller, the image has been converted to a distortion-free compressed image [24].

The compressed file is divided into multiple short data of 0.99k size by sub-packaging. The microcontroller processing unit communicates with the satellite communication module through the serial port to transfer each data packet into SBD format files. The workflow diagram of the central controller communication link is shown in Fig. 4. Each data packet is continuously transmitted to Iridium's server through the global satellite network. The subpacket and compressed data are reorganized on the user-side software in IP port access. The target

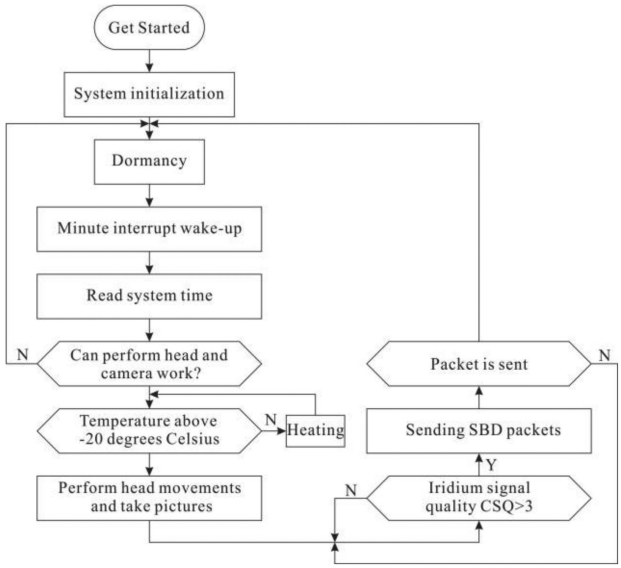

Fig. 4. Main controller communication control flow chart.

outline is made more evident by a defogging enhancement algorithm.

III. Image Defogging and Enhancement Algorithms

The recovery of images acquired by outdoor systems under unfavorable weather conditions is a challenging topic in computer vision, and the application value and prospect of the topic are auspicious. In the long time image monitoring in unmanned areas in the polar field, the acquired images are often affected by the weather, such as snowy and foggy days. This article investigates an improved computer method for recovering images affected by unfavorable weather, and a theoretical basis is provided.

A. Retinex Theory

The earliest proposed theory of the retinal cerebral cortex was presented byLand and McCann in Ohio on December 30, 1963 [25]. Retinex theory is a theory based on the constancy of colour. According to Retinex theory, the color of an object is determined by the object's ability to reflect long-wave (red), medium-wave (green), and short-wave (blue) light, rather than by the absolute value of the intensity of the reflected light. Moreover, the object's color is not affected by the nonuniformity of the light and is consistent, i.e., Retinex is based on color sense consistency. Unlike traditional linear and non-linear image enhancement, the Retinex method can balance dynamic range compression, edge enhancement and color constancy. This results in enhanced adaptiveness for most images. According to Retinex theory, the image acquired by the sensor is considered the product of the ambient incident light and the object's reflection, and the mathematical model is shown in (1) [26]

$$I(x, y) = L(x, y) \cdot R(x, y) \tag{1}$$

where $I(x,y)$ is the acquired image matrix, (x,y)represents the pixel cells of the image matrix, i.e., the spatial position of

the pixels, $L(x,y)$ is the ambient incident light, and $R(x,y)$is the reflected light from the object's surface. The core idea of the Retinex algorithm is to minimize the influence of the incident light in the original image to obtain a reflective image that reflects the characteristics of the image as ultimately as possible.

B. Single-Scale Retinex Defogging Enhancement Algorithm

Depending on the method of approximating the brightness of the image, many different Retinex algorithms have sprung up. The single-scale algorithm was developed based on Jobson and Rahman's proposed centre-surround theory [27], [28]. The mathematical form of the single-scale Retinex algorithm is shown as

$$r_i(x,y) = \log L_i(x,y) - \log\left[S(x,y) * L_i(x,y)\right] \tag{2}$$

where $r(x,y)$ is the output of the single-scale Retinex algorithm at the ith colour channel, the log is the natural logarithm and $S(x,y)$ is the surround function. Equation (2) $S(x,y) * L_i(x,y)$ is considered an estimate of the luminance image $L(x,y)$. In general, the wrap-around function we choose $S(x,y)$is a Gaussian function with the expression

$$S(x,y) = K\exp\left[-\frac{\left(x^2+y^2\right)}{c^2}\right]. \tag{3}$$

In (3), $\boldsymbol{c}$ describes the scale of the Gaussian function. It is from it that the range of the convolution operation is determined. In other words, when the value of $\boldsymbol{c}$ is increased, the overall effect of the image obtained after processing is enhanced, and the colours are closer to the natural effect. However, the problem of minor detail enhancement arises. Conversely, when the value is reduced, the detail enhancement is enhanced, and the dynamic range of the gray scale values is increased, where K is the normalization factor, $S(x,y)$ subject to the normalization condition

$$\int\int S(x,y)dxdy = 1. \tag{4}$$

From the above presentation, the steps for the implementation of the single-scale Retinex algorithm can be obtained as follows.

1) Logarithmic Domain Transformation of Images: The original image is obtained, and the three colour components are converted to the logarithmic domain if it is a colour image; if the input image is a gray-scale image, each pixel of the image is converted to the logarithmic domain.

2) Constructing a Gaussian Kernel Function: Determine the scale parameter c and construct a Gaussian kernel while estimating the value of the parameter K.

3) Output Image: The program converts $r(x,y)$ to the real field and the result $R(x,y)$ is the output image.

The key to Retinex theory is that by assuming the image's composition, the observer sees the image as an image with multiplicative noise. The incident light component is a multiplicative, relatively uniform noise. The Retinex algorithm reasonably estimates the noise at each location and removes it.

C. Multiscale Retinex Defogging Enhancement Algorithm With Colour Recovery Factor C

As can be seen from the image enhancement results, the single-scale Retinex algorithm is difficult to balance between dynamic range compression and colour consistency, so the multiscale Retinex algorithm was created. This allows colour enhancement, local dynamic range compression, and global dynamic range compression.

The multiscale Retinex algorithm is generated after weighting the single-scale Retinex algorithm by several scales

$$R_{\mathrm{MSR}_i} = \sum_{n=1}^{N} w_n R_{ni} \tag{5}$$

In (5), the number of scales is described by N (the general case takes the value of three). R_{ni} is used to describe the results of the single-scale Retinex algorithm for the ith colour channel at the nth scale, w_n is used to describe the weighting coefficients at the nth scale, and R_{MSR_i} is the result of the multiscale Retinex algorithm at the ith colour channel. It can be seen that the scale and number of surround functions have a significant impact on the Retinex algorithm results.

In general, an image with significant differences in brightness within an image subjected to Retinex enhancement is prone to halos. In addition, abrupt shadow boundaries, insufficient edge sharpening, unclear textures, partial colour distortion, lack of significant improvement in detail information in highlight areas and minor sensitivity to highlight areas are some of the more common disadvantages of the Retinex algorithm.

The choice of the number of scales and the scale size of the surround function is an essential factor in determining the enhancement effect of the multiscale Retinex algorithm. As the main focus of this article is on low-quality sea ice images in foggy conditions in ice areas, such images are characterised. Images affected by different weather conditions can produce blurred foreground or background.

As can be seen from the Fig. 5 of the experimental results, the Retinex algorithm expands the range of gray values. It improves the image's contrast so that the detailed information is well preserved, but the processed image still shows some degree of colour distortion. For some small targets, i.e., melting ponds of sea ice or equipment on sea ice, the Retinex multiscale algorithm can defog the image for enhancement.

Based on the above comparative analysis, Fig. 5 shows the processing results with the single-scale Retinex algorithm and with the multiscale Retinex algorithm (where the Gaussian function has scales of 128, 256 and 512), respectively. Fig. 5(a) and (b) shows the original image and its gray-scale image; Fig. 5(c) and (d) shows the image and its gray-scale image after single-scale Retinex processing; Fig. 5(e) and (f) shows the image and its gray-scale image after multiscale Retinex processing. Fig. 5(g)–(i) shows the gray-scale histograms corresponding to the original image, the single-scale Retinex algorithm and the multiscale Retinex algorithm images.

In the Retinex defogging enhancement algorithm described above, both single and multiple scales cause the ratio of the R, G, B channels to change so that the enhancement results will be

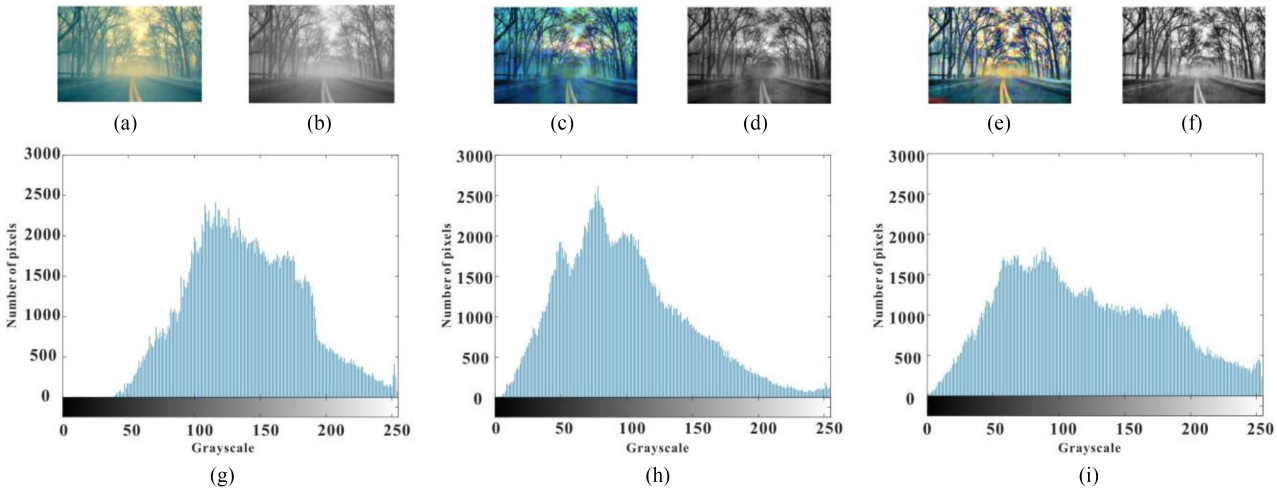

Fig. 5. (a) Original image. (b) Gray-scale image. (c) Original image after single-scale Retinex processing. (d) Original gray-scale image after single-scale Retinex processing. (e) Original image after multi-scale Retinex processing. (f) Original gray-scale image after multi-scale Retinex processing. (g) Gray scale histograms corresponding to the original image. (h) Gray scale histograms corresponding to single-scale Retinex algorithm. (i) Gray scale histograms corresponding to multiscale Retinex algorithm.

distorted to varying degrees. To balance the relationship between the *R, G, B* channels of the colour image and solve the problem of color distortion in the multiscale Retinex algorithm, a color recovery factor *C* [29] is added. The expression for *C* is shown as

$$C_n(x,y) = F\left(\frac{L_n(x,y)}{\sum_{n=1}^{3} L_i(x,y)}\right) \tag{6}$$

where *F* is the mapping function. Where $L_n(x,y)$ represents the average luminance information of the *n*th scale. The multiscale Retinex mathematical expression with a colour recovery factor *C* is shown as

$$R_{\text{msrcr}_i}(x,y) = \sum_{n=1}^{N} C_n \omega_n \log\left(\frac{L_i(x,y)}{S_n(x,y) * L_i(x,y)}\right). \tag{7}$$

D. Combined With the Intelligent Optimized Defogging Enhancement Algorithm ECS-MSRCR

Various swarm intelligence optimisation algorithms exist for the appropriate optimisation of various mathematical problems. 2009 saw the development of the algorithm by Yang and Deb [30] based on the breeding behavior of the cuckoo bird. The cuckoo algorithm focuses on solving optimisation problems by modelling the cuckoo's nestling parasitism and the Levy flight mechanism of specific bird species. Cuckoos rely on other parasitic nests to lay their eggs, and the host bird incubates the eggs as if they were it is own. If the host bird recognises the foreign egg, two events occur; either the egg is thrown away, or it leaves the nest and builds a new one. The cuckoo algorithm is a theory of finding cuckoo by randomly wandering around to find the best nest to incubate the eggs. There are three basic idealised rules involved.

1) Cuckoos arrive at a random nest to lay one egg at a time.
2) The parasitic nest with the highest egg production rate will be carried over to the next generation among randomly selected nests.
3) The number of nests available to the host is fixed, and the probability that the host bird will find an egg laid by a cuckoo is Pa.

Based on the idealized rule, the mathematical expression used by the cuckoo for each generation of the search for an optimal nest location is shown as

$$x_i^{(t+1)} = x_i^{(t)} + \alpha \oplus Levy(\lambda), (i = 1, 2, \ldots n). \tag{8}$$

$x_i^{(t)}$ represents the position of the *i*th nest at generation *t*, $\oplus$ represents point-to-point multiplication, and α represents the step size factor, which controls the step size and usually takes the value 1. Levy(λ)is a random search path generated by a Levy flight obeying the parameter λ. Its move step size obeys the Levy stable distribution. The mathematical expression for Levy is given as

$$\text{Levy} \sim \mu = t^{-\lambda}, \quad 1 < \lambda \leq 3. \tag{9}$$

From (9), it can be seen that the CS algorithm's optimisation path consists of two parts, namely frequent short jumps and occasional long jumps, which makes it easier for the algorithm to jump out of the local optimum.

This article focuses on the defogging and enhancement of images taken on sea ice by the cuckoo search algorithm. In the multiscale Retinex study mentioned above, the determination of the colour recovery factor *C* is a major parameter in improving the defogging and enhancement of the images. The CS algorithm selects the colour recovery factor *C* to enhance the sea ice images.

The study draws on the ECS-enhanced cuckoo search algorithm proposed by Kamoona and Patra [31]. The algorithm achieves automatic image contrast enhancement by optimising the parameters of the local/global transform. Their proposed

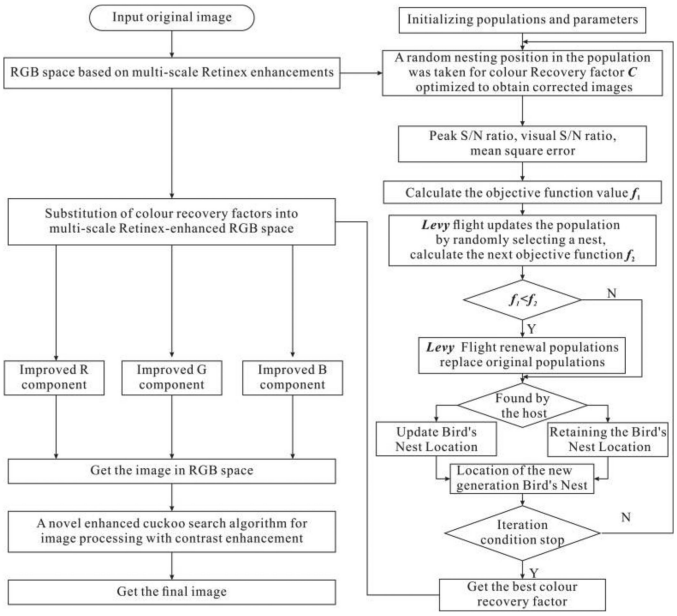

Fig. 6. Flow chart of the intelligent optimised mist elimination enhancement algorithm ECS-MSRCR.

ECS algorithm improves the ability to develop CS to achieve the best solution. In the ECS image enhancement algorithm, an objective function is constructed using entropy, the sum of the number of edges (edge pixels) and the intensity of the edges. The ECS algorithm makes use of the greedy selection method of the *ABC* [32] algorithm to improve search power. The same estimation of the choice of the global optimum solution is required in the optimization process of searching for the local optimum solution [33]. The algorithm has shown good diversification and enhancement capabilities since its introduction. The image processed by the MSRCR algorithm is again subjected to ECS image enhancement to obtain the final target result image.

The general framework of the enhanced approach is shown in Fig. 6.

IV. Experiment

The present visually enhanced long-duration sea ice monitoring system requires many of the functions mentioned above in order to be able to complete a year-long observation of drifting movements with sea ice in the central arctic region. In this article, domestic experiments were conducted to address several of these important functions. The experiments cover the following points.

1) *Equipment Working at Low Temperatures*: The range of low temperatures that the equipment can withstand.
2) *Photo-taking in Extreme Night Conditions*: The ability to monitor the status of the device during extreme night.
3) *Quality Assurance of Image Transmission*: Experiments in image sub-packaging and compression.
4) *Enhancement Experiments on Polar Return Images*: enhancement based on live images.

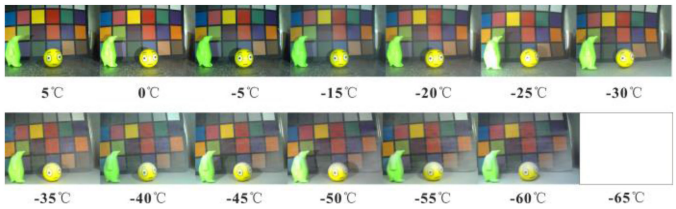

Fig. 7. Low temperature photographic experiments in lighted environments.

A. Systematic Low Temperature and Low Light Conditions Experiments

Having a stable centre of gravity and the necessary buoyancy is necessary for equipment on sea ice in polar regions. In addition, the designer's testing of the low temperature performance of the equipment's improved sensors is a necessary part of the equipment before it is put into service.

In this section, experiments are carried out on self-heating cameras for effective photography in low temperature environments. There are two main types of heated objects, the first targeting the imaging sensor itself for the imaging ambient temperature experiments. The second object is the system controlled heating in addition to the image sensor. As shown in Fig. 7, experiments with a camera simply with a thermistor wire in a refrigerator at low temperatures are demonstrated. The camera in the field is mounted in an IP66 head cover, so in this cryogenic simulation experiment, the camera is placed directly inside the cryogenic refrigerator.

In the low-temperature experiments with the camera, the procedure was to heat the camera when the temperature fell below −25 °C. As shown in Fig. 7, when the ambient temperature reaches −60 °C, the camera's chip is unable to produce an effective image output. The camera therefore meets the ambient temperature operating conditions for the central Arctic region where the temperature is maintained at −40 °C to 5 °C all year round [34].

The second heating object is the heating of the device controller and the battery. The heating method is based on an electric heating plate, where the heating power and the heating strategy are designed with reference to the heating method used by the authors for space environmental sensors in the antarctic interior. The simple thermal network structure of the device is first constructed, and then the heating power strategy is roughly determined for the temperature difference of the device. This is because similar experiments have obtained good precedents for application in Antarctic environments below −50 °C. A related approach can be found in the work of Wang *et al.* [35]. The corresponding heating power as well as the temperature difference (difference between controller temperature and air temperature) are given in Table III.

The power heating stages given in Table III are roughly divided into seven segments. The heating plate has four heating resistors on the front and back sides (eight heating methods). Due to the good thermal conductivity of the heating plate, the battery on one side and the controller on the other side can be heated evenly.

TABLE III
IMPROVED CAMERA PARAMETERS

Temperature Difference (°C)	Input to the System Over 1 h Heat (KJ)	Heating Power (W)
0–5	*0–17.21*	*0–4.78*
5–10	*17.21–34.49*	*4.78–9.58*
10–15	*34.49–51.696*	*9.58–14.36*
15–20	*51.696–68.94*	*14.36–19.15*
20–25	*68.94–87.804*	*19.15–24.39*
25–30	*87.804–103.428*	*24.39–28.73*
30–35	*103.428–120.636*	*28.73–33.51*

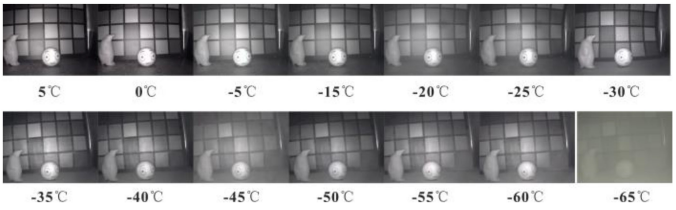

Fig. 8. Cryogenic photographic experiment in a dark environment.

For the low temperature experiment in Fig. 7, the light source inside the fridge was switched off separately and infrared photography was carried out as shown in Fig. 8. It can be seen that the group with infrared filming corresponds to the group with external light sources that could not be filmed at an ambient temperature of −65 °C. This is the case for the group with the external light source.

Combined with the two parallel experiments at low temperatures, the results show that the equipment can operate normally at the ambient temperature of the arctic sea ice and the ambient light level.

B. Experiments in Image Packetization and Compression

The acquisition of images was experimented with in the following section. The acquired images need to be transmitted back to the cloud server side in the country by means of satellite communication. There are corresponding tests in terms of decomposition and reconstruction of the image. This means that the reconstructed image meets the normal image format and that there are no discrepancies between the reconstructed image and the original captured image due to misalignment. Typically, during the domestic experiments, there are several cases where the image reconstruction fails and the program will either repackage the image or resend the image package in response to the failure.

1) *First Type of Situation*: An error occurs before the image is subpackaged, i.e., a file that does not meet the JPEG format is generated, this situation will recommand the camera to take a picture.
2) *Second Scenario*: There are two ways to send the process by satellite, one is the voice dialling method (prone to packet loss) and the other is the SBD short message method (more reliable). For the voice dialling method of image transmission, a lack of data is encountered when transmitting large size images (usually over 30 kb).

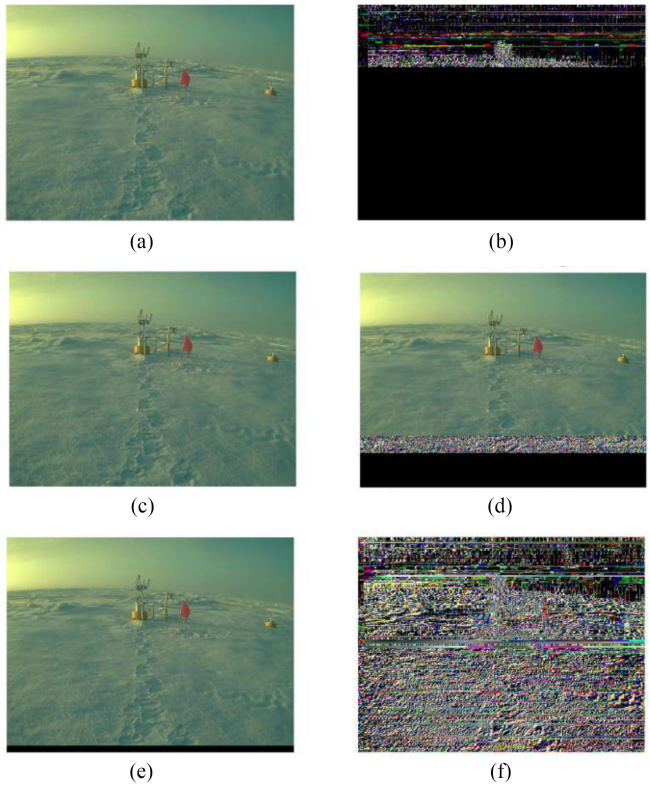

Fig. 9. (a) Successfully transmitted image. (b) Image after one byte missing in the middle of the image data. (c) Image with one byte missing at the end of the image data. (d) Images missing a whole packet (this case is for SBD transmissions and the program is set to 1 kb per packet), which is located in the middle of the data. (e) Images missing a whole packet (this case is for SBD transmissions and the program is set to 1 kb per packet), which is located in the end of the data. (f) Image with one wrong byte.

In this article, simulated experiments were done for the failure of voice dialling as well as SBD transmission methods. By setting up an experimental result filtering procedure, the server side was able to filter and classify the failed images. Such unsuccessful transmissions are broadly classified into the following five categories as shown in Fig. 9, which contains the following cases: successful transmissions; one byte missing from the middle of the image data; one byte missing from the end of the image data; images missing a whole packet (this case is for SBD transmissions and the program is set to 1 kb per packet), which is located in the middle of the data; a whole packet of images is missing (this is for SBD transmission and the program is set to 1 kb per packet) and the packet is located at the end of the data; and an image with an error byte is present.

In order to improve the efficiency and quality of image acquisition in the field, this system uses image compression technology. The advantages of using this technique are that more images are acquired at a certain point in time with a limited transmission length of communication bytes, and that the compressed data has a low probability of image failure due to packet loss because of its short length. The compressed image is one-tenth the size of the original image. This results in a significant saving in communication costs and transmission

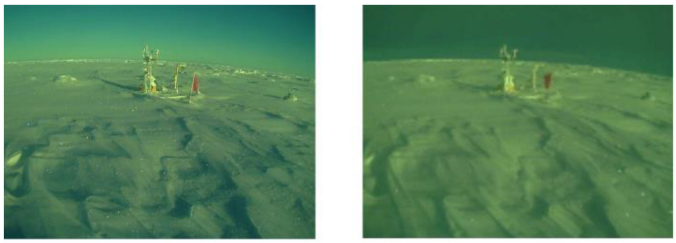

(a) (b)

Fig. 10. Schematic of image compression comparison from the field.

time. A comparison of the images before and after compression is shown in Fig. 10.

C. Defogging Enhancement Comparison Test

Experiments were conducted to enhance post-return images for different sea fog, low brightness, and unclear edges. The authors' aim was to select a suitable defogging algorithm to highlight the unmanned integrated sea-ice profiling system/sea-ice melt pond. The images used in the experiments were arctic field acquired data and images with similar characteristics.

The author used two performance metrics in order to measure the quality of the ECS-MSRCR enhanced images proposed in this article and to compare it with other algorithms. These performance measures are: peak signal-to-noise ratio (PSNR) and feature similarity index mersure (FSIM).

Mean square error (MSE) is a relatively common quality evaluation method that measures the quality of the image to be evaluated statistically by calculating the difference between the gray scale values of the corresponding pixel points of the image to be evaluated and the reference image. The formula for calculating MSE is as follows:

$$\mathrm{MSE} = \frac{1}{N}\sum_{i=1}^{N} E_i^2 = \frac{\| \boldsymbol{E}\|^2}{N} \tag{10}$$

where E is the difference between the reference image and the image to be evaluated, E_i is the ith pixel difference and N is the number of pixels in the image. However, the MSE does not reflect the visual quality of the image well because it does not take into account the visual characteristics of the human eye.

As higher values of quality indicators generally mean better quality, the MSE is transformed to obtain the PSNR indicator. The formula is as follows [36]:

$$\begin{aligned}\mathrm{PSNR} &= 10\log_{10}\left(\frac{(2^n-1)^2}{\mathrm{MSE}}\right)\\ &= 20\log_{10}(2^n-1) - 20\log_{10}\left(\frac{\| E\|}{\sqrt{N}}\right).\end{aligned} \tag{11}$$

A higher PSNR value indicates less distortion.

FSIM indicates the similarity of features between the reference image and the image to be measured. The higher the FSIM value, the more similar the reference image and the image to be measured are, the higher the quality of the image to be measured is, and vice versa, the poorer the quality of the image to be measured is. If f_1(x) represents the original image,and f_2(x) represents the enhanced image. FSIM [37] defined as

(a) (b) (c)

Fig. 11. (a) Experimental control group—fog diagram. (b) Experimental control group—sea ice equipment diagram. (c) Experimental control group—sea ice diagram.

$$\mathrm{FSIM} = \frac{\sum_{x\in\Omega} S_L(x)\cdot PC_m(x)}{\sum_{x\in\Omega} PC_m(x)} \tag{12}$$

$$S_L(x) = S_{PC}(x)\cdot S_G(x) \tag{13}$$

$$PC_m(x) = \max\left(PC_1(x), PC_2(x)\right) \tag{14}$$

$$S_{PC}(x) = \frac{2PC_1(x)\cdot PC_2(x) + T_1}{PC_1^2(x) + PC_2^2(x) + T_2} \tag{15}$$

$$S_G(x) = \frac{2G_1(x)\cdot G_2(x) + T_1}{G_1^2(x) + G_2^2(x) + T_2} \tag{16}$$

where Ω denotes the entire null field. S_{PC} (x) represents the feature similarity of images f_1 (x) and f_2 (x). S_L (x) represents the local similarity of f_1 (x) and f_2 (x) at pixel location x. S_G (x) represents the gradient similarity of images f_1 (x) and f_2 (x). The phase consistency information of images f_1 (x) and f_2 (x) is represented by $PC_1(x)$ and $PC_2(x)$, respectively. $G_{\mathrm{i}}(x)$ denotes the gradient amplitude of the reference image and the image to be measured; T_1 and T_2 are constants.

Both the reference image and the image to be measured were evaluated for quality according to the gray-scale image. The experiments in this section are divided into a total of three control groups for the single scale Retinex (SSR) proposed in Section B, the multiscale Retinex (MSR) proposed in Section III-C and the ECS-MSRCR image enhancement method proposed in Section III-D. The evaluation criteria refer to the two criteria proposed in this section. The reference images used for the control group, respectively, were.

1) Common foggy sky image.
2) Image of sea ice equipment taken by this system.
3) Image of a sea ice melting pond taken by this system.

The RGB and gray-scale plots of the three images are shown in Fig. 11.

Nine sets of experiments were conducted in this experiment with three control groups as shown in Fig. 12. The results for control group one are given in Table IV, the results for control group two are given in Table V and the results for control group three are given in Table VI. The results of the image enhancement

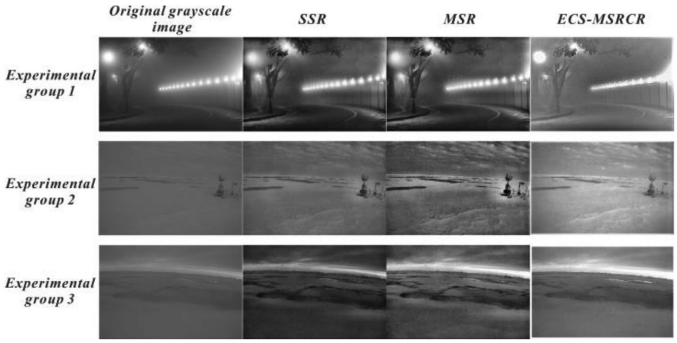

Fig. 12. Comparison of image enhancement results.

TABLE IV
COMPARISON OF FOG MAP ENHANCEMENT RESULTS-GROUP1

Algorithms	**PSNR**	**FSIM**
SSR	*21.216*	*0.8587*
MSR	*17.36*	*0.8974*
ECS-MSRCR	*20.232*	*0.9093*

TABLE V
COMPARISON OF FOG MAP ENHANCEMENT RESULTS-GROUP2

Algorithms	**PSNR**	**FSIM**
SSR	*26.72*	*0.8722*
MSR	*16.1523*	*0.8826*
ECS-MSRCR	*7.041*	*0.885*

TABLE VI
COMPARISON OF FOG MAP ENHANCEMENT RESULTS-GROUP3

Algorithms	**PSNR**	**FSIM**
SSR	*16.373*	*0.8180*
MSR	*13.264*	*0.8687*
ECS-MSRCR	*14.6*	*0.8733*

comparison of the nine sets of experiments for the three control groups are shown in Fig. 12.

It can be seen that the ECS-MSRCR method results in less distortion and more structural similarity in the enhancement of images with fog or unclear contour features. As shown in Fig. 12, MSR is more effective than ECS-MSRCR for contour enhancement, but the corresponding structural similarity decreases and distortion increases. The choice of MSR or ECS-MSRCR enhancement method is based on the actual requirements. The algorithm proposed in this article is used if enhancement is required and distortion is not too high.

V. FIELD INTERANNUAL MONITORING

A. Systematic Overall Drift Trajectory and Start/Stop Information

The system spent 356 days in the polar region and arrived at a sea area at 86.0456832°N, 162.5763456°E on August 21, 2020

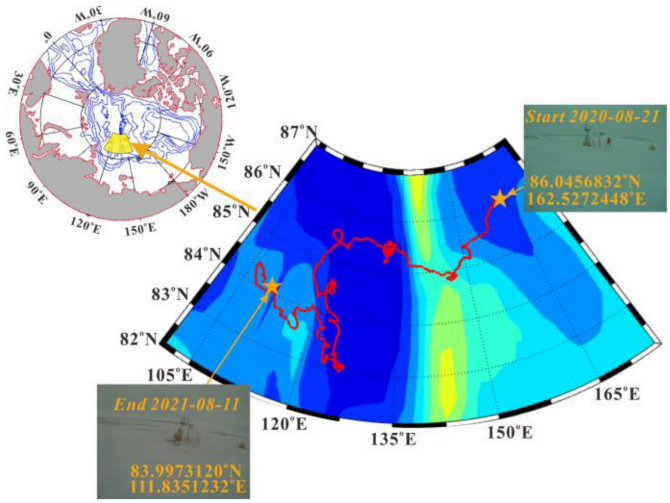

Fig. 13. Sea ice monitoring system with information on the drift paths and starting systems of the larger systems in which it operates.

with the 11th Chinese Arctic scientific expedition and carried out the deployment mission. It experienced an ice age in the Arctic, drifting with a fixed ice floe between 83°N and 86°N. In total, 40.21 M of image information was returned, along with status information. Due to the collapse of the sea ice and melting of the ice in the following summer, the system returned several successive short alert messages of falling voltage values after the last image was returned on August 11, 2021, and then lost communication before returning no more data. The starting and ending positions are marked by stars as shown in Fig. 13, and the system reaches a northernmost point of about 86°N, a southernmost point of about 83°N, an easternmost point of about 105°E and a westernmost point of about 165°E during the year.

B. Summary of Representative Images Captured During Interannual Monitoring

A total of 273 photographs were taken of the system between the official launch and the mechanical damage to the system caused by the collapse of the sea ice. Of these, very low temperature conditions resulted in heavy ice and snow cover on the equipment (which could not be cleared by lens wipers as well as head rotation). A selection of images from the monitoring during different periods of sea ice are summarised in Fig. 14. Each image is labeled with the time it was taken in the top left hand corner and the geographical location of the sea ice at that time in the bottom right hand corner. August 21, 2020 the installer left the system to begin operation under the control of in-country personnel. On September 21, 2020 polar bear footprints were photographed walking from the monitoring device to the monitored device. When the system enters the northern hemisphere winter, i.e., the period from January 27, to May 2, 2021. Snow and ice cover buried the viewport and can be seen covering the equipment being photographed in the photograph from May 2, 2021. In the images from November and around May, it can be seen that the images are progressively blurred and then gradually clarified. It is possible to speculate that the frost

Fig. 14. Excerpts from interannual photographs taken by the sea ice image monitoring system.

may have covered the viewport. The first time a melting pond was seen on the image was on July 15 and the following month, the pattern of the melting pond changed rapidly and the image taken on August 8, 2021 shows that the equipment being monitored was already tilted. After the voltage status was transmitted back on August 15, 2021, no response from the system.

VI. Conclusion

In this article, the feasibility of using real-time image monitoring equipment in a cold sea ice environment is assessed. Throughout the experimental and theoretical description sections, the feasibility of using small to medium sized image monitoring devices in a cold arctic sea ice environment is evaluated and validated. In conjunction with domestic and arctic field implementations, the ambient operating temperatures for the visible output of the CMOS serial camera and the infrared output in dark environments are below the temperature range band described in the equipment manual. For small size (a few kb to tens of kb) images, the article proposes a visual enhancement algorithm suitable for this type of image. Two approaches and means were derived in the experiments that are applicable to image processing. These are the MSR algorithm model and the ECS-MSRCR algorithm model proposed in this article. The structural similarity of the relevant enhanced experimental images done in the captured images is maintained above 0.87. The work done on the breakpoint transmission of images sent in packets has not yet found a similar solution in a similar product for the relevant arctic sea ice centre region. Three modes of photo transmission were used in this article: small-scale image transmission (3 kb); medium-scale transmission (30 kb); and large-scale transmission (300 kb). The small and medium scale image transfer is used predominantly in routine monitoring to meet the image requirements for identifying the state of the structure outside the equipment as well as changes in the physical state of the sea ice. The power consumption of the image detection device and its accompanying drive unit is around 12 W in full operating mode, 245 mW in normal shooting mode (no rotation of the head) and 1.2 mW in sleep mode. Every three days, four images (with different angles of gimbal rotation and 35–40 s of rotation time) are taken and returned in 3 kb, during which time the battery power is evaluated and the choice is made whether or not to transfer medium to large scale images. So, the battery equipped is 1800 W hours. The estimated PV output in summer varies from 0.3 to 1 W, so the power for system work in summer can be covered by the PV unit. The whole system can theoretically achieve at least one year of operation without the structure being damaged by sea ice. Future work will focus on evaluating the stability of the sea ice image monitoring equipment during long-term operation and the ability of the system to learn to capture points of interest autonomously. In order to further determine the feasibility of this sea-ice drift image observation system. To provide closer, more interesting to researchers and more complete time series of sea ice imagery observations.

References

[1] T. V. Callaghan, M. Johansson, T. D. Prowse, M. S. Olsen, and L. O. Reiersen, "Arctic cryosphere: Changes and impacts," *Ambio*, vol. 40, pp. 3–5, Dec. 2011.

[2] M. S. Olsen *et al.*, "The changing arctic cryosphere and likely consequences: An overview," *Ambio*, vol. 40, pp. 111–118, Dec. 2011.

[3] W. Maslowski, J. C. Kinney, J. Jakacki, R. Osinski, and J. Zwally, "Arctic sea ice thickness distribution as an indicator of arctic climate change - Synthesis of model results and observations," in *Proc. EGU Gen. Assem. Conf. Abstr.*, 2010.

[4] K. J. Campbell, "A continuous profile of sea ice and freshwater ice thickness by impulse radar," *Polar Rec.*, vol. 17, no. 106, pp. 31–41, 1974.

[5] R. Timmermann, S. Danilov, J. Schrter, C. Bning, D. Sidorenko, and K. Rollenhagen, "Ocean circulation and sea ice distribution in a finite element global sea ice–ocean model," *Ocean Model.*, vol. 27, no. 3–4, pp. 114–129, 2009.

[6] M. J., P. Walker, and W. Penney, "Arctic sea-ice and maritime transport technology," *Weather*, vol. 28, pp. 358–371, 1973. [Online]. Available: https://doi.org/10.1002/j.1477-8696.1973.tb00838.x

[7] S. Gerland *et al.*, "Essential gaps and uncertainties in the understanding of the roles and functions of Arctic sea ice," *Environ. Res. Lett.*, vol. 14, no. 4, Apr. 2019, Art. no. 043002.

[8] J. A. Maslanik *et al.*, "A younger, thinner Arctic ice cover: Increased potential for rapid, extensive sea-ice loss," *Geophys. Res. Lett.*, vol. 34, pp. 497–507, 2007. [Online]. Available: https://doi.org/10.1029/2007GL032043

[9] J. Maslanik, J. Stroeve, C. Fowler, and W. Emery, "Distribution and trends in Arctic sea ice age through spring 2011," *Geophys. Res. Lett.*, vol. 38, Jul. 2011, Art. no. L13502.
[10] S. Y. Liu *et al.*, "Changes in the global cryosphere and their impacts:A review and new perspective," *Cold Regions Sci. Technol.*, vol. 12, no. 6, pp. 343–354, 2020.
[11] M. Wang and J. E. Overland, "A sea ice free summer arctic within 30 years: An update from CMIP5 models," *Geophys. Res. Lett.*, vol. 39, Sep. 2012, Art. no. L18501.
[12] J. Du *et al.*, "Remote sensing of environmental changes in cold regions: Methods, achievements and challenges," *Remote Sens.*, vol. 11, no. 16, Aug. 2019, Art. no. 1952.
[13] N. Ivanova *et al.*, "Retrieval of Arctic sea ice parameters by satellite passive microwave sensors: A comparison of eleven sea ice concentration algorithms," *Geosci. Remote Sens.*, vol. 52, no. 11, pp. 7233–7246, 2014.
[14] A. Bhardwaj, L. Sam, Akanksha, F. J. Martin-Torres, and R. Kumar, "UAVs as remote sensing platform in glaciology: Present applications and future prospects," *Remote Sens. Environ.*, vol. 175, pp. 196–204, Mar. 2016.
[15] R. Lei, P. Heil, J. Wang, Z. Zhang, Q. Li, and N. Li, "Characterization of sea-ice kinematic in the Arctic outflow region using buoy data," *Polar Res.*, vol. 35, 2016, Art. no. 22658.
[16] C. J. Planck, J. Whitlock, C. Polashenski, and D. Perovich, "The evolution of the seasonal ice mass balance buoy," *Cold Regions Sci. Technol.*, vol. 165, Sep. 2019, Art. no. 102792.
[17] Z. Liao *et al.*, "Snow depth and ice thickness derived from SIMBA ice mass balance buoy data using an automated algorithm," *Int. J. Digit. Earth*, vol. 12, no. 8, pp. 962–979, Aug. 2019.
[18] Y. Cheng *et al.*, "Air/snow, snow/ice and ice/water interfaces detection from high-resolution vertical temperature profiles measured by ice mass-balance buoys on an Arctic lake," *Ann. Glaciol.*, vol. 61, no. 83, pp. 309–319, Dec. 2020.
[19] B. Cheng *et al.*, "Evolution of snow and ice temperature, thickness and energy balance in Lake Orajärvi, northern Finland," *Tellus A, Dyn. Meteorol. Oceanogr.*, vol. 66, no. 1, 2014, Art. no. 21564.
[20] M. Hoppmann *et al.*, "Seasonal evolution of an ice-shelf influenced fast-ice regime, derived from an autonomous thermistor chain," *J. Geophys. Res., Oceans*, vol. 120, no. 3, pp. 1703–1724, 2015.
[21] S. Gani, J. Sirven, N. Sennéchael, and C. Provost, "Revisiting winter Arctic ice mass balance observations with a 1-D model: Sensitivity studies, snow density estimation, flooding, and snow ice formation," *J. Geophys. Res., Oceans*, vol. 124, no. 12, pp. 9295–9316, 2019. [Online]. Available: https://doi.org/10.1029/2019JC015431
[22] R. Treffeisen, R. Krejci, J. Strom, A. C. Engvall, A. Herber, and L. Thomason, "Humidity observations in the Arctic troposphere over Ny-Alesund, Svalbard based on 15 years of radiosonde data," *Atmos. Chem. Phys.*, vol. 7, no. 10, pp. 2721–2732, 2007.
[23] B. Su, K. Riska, and T. Moan, "A numerical method for the prediction of ship performance in level ice," *Cold Regions Sci. Technol.*, vol. 60, no. 3, pp. 177–188, Mar. 2010.
[24] G. K. Wallace, "The JPEG still picture compression standard," *IEEE Trans. Consum. Electron.*, vol. 38, no. 1, pp. 30–44, Feb. 1992, doi: 10.1109/30.125072.
[25] E. H. Land and J. J. McCann, "Lightness and retinex theory," *J. Opt. Soc. Amer.*, vol. 61, no. 1, pp. 1–11, 1971.
[26] J. Wang *et al.*, "Image processing technology in fog and haze environment based on Retinex theory," in *Proc. Int. Conf. Comput.*, 2018.
[27] D. J. Jobson, Z. U. Rahman, and G. A. Woodell, "A multiscale retinex for bridging the gap between color images and the human observation of scenes," *IEEE Trans. Image Process.*, vol. 6, no. 7, pp. 965–976, Jul. 1997, doi: 10.1109/83.597272.
[28] D. J. Jobson, Z. U. Rahman, and G. A. Woodell, "Properties and performance of a center/surround retinex," *IEEE Trans. Image Process.*, vol. 6, no. 3, pp. 451–462, Mar. 1997, doi: 10.1109/83.557356.
[29] J. Zhou, J. Yao, W. Zhang, and D. Zhang, "Multi-scale retinex-based adaptive gray-scale transformation method for underwater image enhancement," *Multimedia Tools Appl.*, vol. 81, no. 2, pp. 1811–1831, Jan. 2022.
[30] X.-S. Yang and S. Deb, "Cuckoo search via levey flights," in *Proc. World Congr. Nature Biol. Inspired Comput.*, 2009, pp. 210–214. [Online]. Available: //WOS:000288686500036
[31] A. M. Kamoona and J. C. Patra, "A novel enhanced Cuckoo search algorithm for contrast enhancement of gray scale images," *Appl. Soft Comput.*, vol. 85, 2019, Art. no. 105749.
[32] D. Karaboga and B. Basturk, "A powerful and efficient algorithm for numerical function optimization: Artificial bee colony (ABC) algorithm," *J. Glob. Optim.*, vol. 39, no. 3, pp. 459–471, Nov. 2007, doi: 10.1007/s10898-007-9149-x.
[33] X.-S. Yang, "Nature-inspired optimization algorithms: Challenges and open problems," *J. Comput. Sci.*, vol. 46, Oct. 2020, Art. no. 101104.
[34] P. D. Jones, D. H. Lister, T. J. Osborn, C. Harpham, M. Salmon, and C. P. Morice, "Hemispheric and large-scale land-surface air temperature variations: An extensive revision and an update to 2010," *J. Geophys. Res.-Atmos.*, vol. 117, Mar. 2012, Art. no. D05127.
[35] Y. Wang, Y. Dou, J. Guo, and D. Huang, "Space physical sensor protection and control system based on neural network prediction: Application in Princess Elizabeth area of Antarctica," *Sensors*, vol. 20, no. 17, Sep. 2020, Art. no. 4662.
[36] Z. C. Ni, Y. Q. Shi, N. Ansari, and W. Su, "Reversible data hiding," *IEEE Trans. Circuits Syst. Video Technol.*, vol. 16, no. 3, pp. 354–362, Mar. 2006, doi: 10.1109/tcsvt.2006.869964.
[37] L. Zhang, L. Zhang, X. Mou, and D. Zhang, "FSIM: A feature similarity index for image quality assessment," *IEEE Trans. Image Process.*, vol. 20, no. 8, pp. 2378–2386, Aug. 2011.

Yuchen Wang received the B.S. degree in electrical engineering from the Taiyuan University of Technology (TUT), Shanxi, China, in 2018.

He studied for a Doctorate in electrical engineering with the Taiyuan University of Technology in July 2019. From 2016 to 2017, he was the Campus Leader of the Siemens Intelligent Manufacturing Challenge of Taiyuan University of Technology; from 2019 to 2020, he participated in the inland team of China's 36th Antarctic Scientific Expedition, from 2021 to 2023, he participated in the winter team of China's 38th Antarctic Scientific Expedition.

Yinke Dou was born in Fengxiang, Shaanxi, in 1973. He received the bachelor's degree in engineering, the master's degree in monitoring technology and automation, and the Ph.D. degree in engineering in circuits and systems from the Taiyuan University of Technology, Shanxi, China, in 1997, 2005, and 2010, respectively. Where he received the Doctorate degree in engineering.

He was a Doctor, a Professor, and a Doctoral Supervisor with Taiyuan University of Technology.

Jingxue Guo received the B.Sc. degree in applied geophysics from Jilin University, Changchun, China, in 2002, and the Ph.D. degree in earth exploration and information technology from Jilin University, Changchun, China, in 2002 and 2007, respectively.

He is currently a Senior Engineer of Polar Geophysical Observation and Research on Cryosphere Changes, Polar Research Institute of China, Shanghai, China.

His research interest includes mainly to apply a variety of geophysical techniques to observe the characteristics of the polar cryosphere, including polar oceans, sea ice, ice sheets, ice shelves, and subglacial geological structures.

Zhe Yang received the B.S. degree in computer science from the Taiyuan University of Technology (TUT), Shanxi, China, in 2017. He is currently working toward the M.Eng. degree with the School of Computer Science, The University of Manchester, Manchester, U.K.

He is currently working on Swarm intelligence algorithm and machine learning.

Bo Yang received the B.S. degree in electrical engineering from the Taiyuan University of Technology, Shanxi, China, in 2019, where he is currently working toward the Doctorate degree in electrical engineering.

Yang Sun received the B.S. degree in petroleum geology from the China University of Petroleum, Beijing, China, in 2009 and the master's degree in geology from Uppsala University, Uppsala, Sweden, in 2019.

He was an Engineer in petroleum geophysics in Beijing, China, for three and half years from 2012 and as a Project Manager with Institute of Deep Sea Science and Engineering, Sanya, China, for one year from 2020. He is currently with Polar Research institute of China Shanghai, Shanghai, China. As an Engineer in glacier hydrology, he focus in the changes in hydrological environment related to lakes and glaciers in Antarctica and their influences on global climate change.

Weixin Liu received the B.S. degree in atmospheric science from the Nanjing University of Information Science and Technology, Nanjing, China, in 2011.

He is mainly involved in atmospheric sounding and weather forecasting services.